Stability Analysis of a WaterRich Slope Under Seismic Disturbance

Wiley
Advances in Civil Engineering
Volume 2024, Article ID 8894948, 13 pages
https://doi.org/10.1155/2024/8894948

WILEY

Research Article

Stability Analysis of a Water-Rich Slope Under Seismic Disturbance

Shujian Li[1], **Yisha Pan**[2], **Chongyang Wang**[3,4], **Dongming Zhang**[3,4], **Bin Zhang**[1], **and Ziyang Xiong**[3,4]

[1]*Yunnan Phosphate Chemical Group Co., Ltd., Kunming 650600, Yunnan, China*
[2]*School of Surveying and Land Information Engineering, Henan Polytechnic University, Jiaozuo 454000, Henan, China*
[3]*State Key Laboratory of Coal Mine Disaster Dynamics and Control, Chongqing University, Chongqing 400030, China*
[4]*School of Resources and Safety Engineering, Chongqing University, Chongqing 400044, China*

Correspondence should be addressed to Chongyang Wang; wcy@cqu.edu.cn

Received 10 July 2024; Accepted 20 September 2024

Academic Editor: Xueping Fan

Studying slope stability under different water contents and stress conditions is very important for the early warning and prevention of slope disasters. In this study, the stability of a side slope in Xingwen County was studied via field investigations, laboratory tests, and numerical simulations. The results show that a dry sample has a greater rockburst proneness than a water-rich sample. Compared with that of the dry sample, the strength of the sample representing the water-rich area of the slope decreased significantly, the peak strength decreases by 28.5% on average under the different confining pressure conditions tested, and the stress–strain curve has more jitter after the peak and shows more obvious plastic characteristics. The peak shear strain in the *XZ* direction on the lower slope under water-rich conditions is 48.5% greater than that under dry conditions, and the range of the slope plastic zone is also significantly greater than that under dry conditions. This indicates that the stability of the slope under water-rich conditions is much lower than that under dry conditions. The safety factors of the three types of slopes are calculated. The slope safety factors under the "water-rich and deadweight" and "water-rich and earthquake" conditions are 3.1% and 5.4% lower, respectively, than that under the "dry and deadweight" conditions. Therefore, it is necessary to strengthen the protection of water-rich areas on slopes with frequent microearthquakes.

Keywords: numerical simulation; slope; stability analysis; triaxial compression test; uniaxial compression test

1. Introduction

Landslides are among the most common geological disasters, but they are difficult to predict and can result in destruction. The occurrence of landslide disasters not only causes the loss of personnel and property within a certain range but also affects traffic, commerce, and daily life. Rainfall and earthquake disturbances can affect the stability of slopes, reduce the safety coefficient of slopes, and increase the probability of slope disasters. Therefore, studying the stability of slopes under water-rich conditions and seismic disturbance is highly important.

The occurrence of landslide disasters requires certain geological conditions, such as steep mountain slopes and loose rock (soil) bodies, as well as the influences of rainfall, earthquakes, and engineering activities [1–7]. The actual area affected by landslides during earthquakes depends on the local lithology, terrain, climate, vegetation coverage, and other factors [8–11]. Senthilkumar, Chandrasekaran, and Maji [12] used the finite difference method to study the effect of rainfall infiltration on unsaturated residual soil slopes and noted that rainfall increased soil saturation and percolation force, formed positive pore water pressure, and thus reduced the shear strength of soil along the soil–rock interface, which easily led to the occurrence of landslides.

Many scholars have predicted and evaluated slope stability under the influence of earthquakes through different models.

Qin and Chian [13] proposed a graphical method related to the G-line to evaluate seismic slope stability. Under kinematic analysis, the safety factor for a particular slope was estimated by determining the G-line. The evaluation of slope stability usually includes quantitative and qualitative methods. Xu, Gorum, and Tanyas [14] used remote sensing and GIS technology to identify and monitor earthquake-induced slope instability, and the results of related projects played a great role in evaluating earthquake-induced landslide susceptibility, landslide evolution, and debris flows in earthquake-affected areas. Wu et al. [15] established four slope models based on relevant factors to simulate and estimate the sensitive landslides and landslide evolution caused by extreme rainfall and noted that most landslides after heavy rainfall were riparian landslides caused by rivers. Samia et al. [16] quantified the priority of landslides at sites with previous landslides, the duration at which such effects were apparent, and the correlation of slope stability with time. The overlap between landslides shows an obvious legacy effect (path dependence), which has an impact on the landslide-affected area. To study the initiation mechanism of bedded rock landslides during earthquakes, Zhao et al. [17] used the fracture mechanics principle to analyze the geometric and stress conditions for initial crack propagation at the back of landslides and deduced the initiation speed of slope instability under the combined effect of the elastic impact, peak residual strength drop, and fluctuations in other metrics.

In the study of slope stability, the results of many laboratory tests provide scientific guidance [18–24]. The application of physical and mathematical evaluation models provides technical support for slope stability analysis [25–28]. Wang et al. [29] conducted in-depth discussions on the development characteristics, activity characteristics, formation and evolution process of landslides based on mapping monitoring, laboratory tests, and numerical simulation analysis and noted that the formation and evolution of landslides in flow slopes were dominated by active neotectonic movement. The continuous deterioration of rainfall, the seismic cracking effect of historical strong earthquakes, and the fracture creep effect are the main factors inducing slope instability. Broeckx et al. [30] evaluated the performance of fitting a multivariate logistic regression model on a subset of independent landslides selected from the total dataset; by simulating the sensitivity of the slope, they observed a significant positive relationship between slope stability and sediment yield, but the relationship was relatively weak. Yang et al. [31], based on the field investigation of the Wenchuan earthquake landslide disaster and vibration table test analysis of unilateral, bilateral, and four-sided slopes, concluded that the amplification of peak acceleration gradually increased with increasing slope angle. Under the influence of earthquakes, slope instability mainly occurred in slopes with slope angles greater than 45°. Zhang et al. [18] carried out a slope stability simulation study by means of a numerical analysis method combined with strength reduction to compare the landslide stacking slope shape and ripple range and performed a back analysis of the strength index in the process of landslide movement.

Although the abovementioned scholars have conducted many simulations and explorations on slope stability through field monitoring, laboratory test, and numerical simulation, there are few studies on the stability of water-rich slopes under seismic stress disturbances. In real-world scenarios, the mechanical properties of slope rock masses, rainfall, and seismic activities significantly impact slope stability. Therefore, it is crucial to explore these parameters (such as mechanical properties of slope rock masses, displacement distribution on slope surfaces, and safety factors) under varying conditions. These investigations are essential for effective slope protection and remediation. This study used laboratory tests and numerical simulations to explore the stability of water-rich slopes under microseismic action. First, samples were collected from the dry and water-rich areas of the slopes in Xingwen County and processed into standard cylindrical samples in the laboratory. Then, uniaxial compression tests and triaxial compression tests were carried out to analyze the mechanical properties of the slope rock mass under dry and saturated conditions. On this basis, the slope model was established by FLAC^{3D} software to analyze the distribution of stress and deformation of dry slopes and water-rich slopes under microseismic disturbance. Areas prone to deformation were found, and protection suggestions were proposed. Then, the safety factor of the slope was calculated under three conditions using the strength reduction method, providing theoretical support for engineering construction and geological disaster prevention.

2. Data Sources and Overview of the Study Area

2.1. Study Area Overview. Yibin city is in Xingwen County in Sichuan Province, located in the transition zone between the southern mountains of Sichuan and the Yunnan–Guizhou Plateau. Xianfeng Mountain divides the county into two branches, with the northern part of the county being low and the southern part being high. Its geographical coordinates are 104°52′28″–105°21′23″ east longitude and 28°04′28″–28°27′18″ north latitude, with a total area of 1379.89 km^2. Xingwen County has a subtropical monsoon climate, abundant rain, surface carbonate rocks generated by long-term water dissolution, and karst landform development. The regional geological structure belongs to the east–west structural system of the southern Sichuan fold belt and is part of the Huaying Mountain seismic belt, which is a fault belt with frequent earthquakes. Rocks are broken under the influence of seismic factors, and geological disasters occur frequently [32]. The Triassic strata in the region are the most widely distributed in the territory, and the bedrock lithology is mainly sandstone, limestone, and marl. The complex geological environment conditions in Xingwen County are influenced by earthquakes, rainfall, human activities, and other factors, and the types of geological disasters vary but include landslides and collapses.

2.2. Data Sources. Digital elevation model (DEM) data were downloaded from the geospatial Data Cloud Platform of the Computer Network Information Center, Chinese Academy of Sciences (http://www.gscloud.cn), and historical disaster

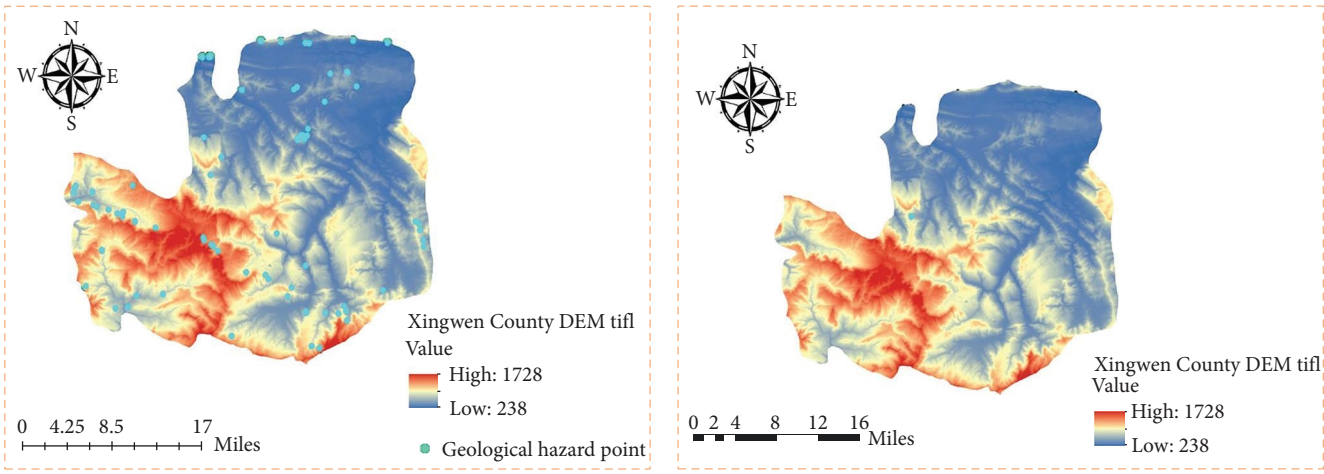

FIGURE 1: Geological map of Xingwen County. (a) Distribution map of geological disasters. (b) Sampling site of the landslide point. DEM, digital elevation model.

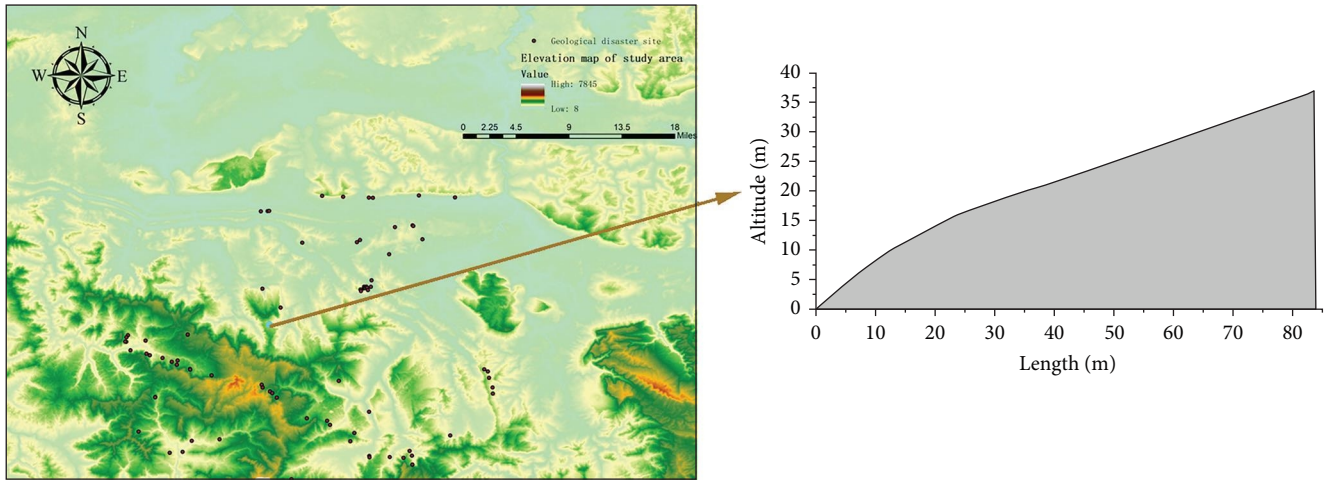

FIGURE 2: Topographic map of the study area and section diagram of the landslide points.

data points were downloaded from Resources and Environmental Science and Data Center, Institute of Geographic Sciences and Natural Resources Research, Chinese Academy of Sciences (http://www.resdc.cn).

As shown in Figure 1, there were 85 geological disaster data points and 59 landslides in Xingwen County in 2020, accounting for 69% of the total number of geological disasters. The numbers of small landslides, medium landslides, and large landslides were 20, 37, and 2, respectively. To explore the influence of geological structure activities on slope stability, the landslide areas were selected for further exploration. Figure 2 shows the geological disaster points from Xingwen County, Sichuan Province. The structure is the southwest wing of the Longqiao anticline. The main lithology is limestone; the groundwater is in the upper stagnation layer.

To analyze the stability of the landslide points in the study area, we obtained limestone samples through field sampling and carried out laboratory experiments. Laboratory tests and numerical simulation calculations were carried out on the samples in the study area to explore their physical and mechanical properties and analyze their stability. Figure 2 shows the 3D topographic map of the study area, and the cyan dots are the sampling sites. The section map of the landslide points was extracted according to the elevation data of the study area and the field conditions.

3. Laboratory Test

3.1. Sample Preparation

3.1.1. Sample Preparation. At the sampling points in the study area, which are affected by rainfall, stagnant water, and surficial broken rock and soil, the stability of the soil is poor, and the soil easily slips. Therefore, the intact sample from the sampling point was processed in the laboratory to make a standard cylindrical sample of Φ 50 × h 100 mm. The processed samples were divided into two groups: a dry group and a water-rich group.

(a) (b) (c)

FIGURE 3: Sample processing and physical property testing device: (a) 101-2SB electric thermostatic drying oven, (b) Nj-BSJ Concrete vacuum satiating machine, and (c) UTA2001A ultrasonic inspection monitor.

TABLE 1: Physical properties of the dry and water-rich samples.

Group	m (g)	ρ (g/cm^3)	v (m/s)
Dry group	416.05	2.12	2564
Water-rich group	522.03	2.66	3154

For the dry group, the samples were placed in an oven (Figure 3a), dried at 45°C for more than 48 h, and removed after the mass became stable.

For the water-rich group, the sample was placed in a vacuum satiating machine (Figure 3b), saturated with water for more than 48 h, and removed after its mass became stable.

The physical properties of the treated samples are shown in Table 1. In Table 1, the P wave velocity of the sample was measured by UTA2001A ultrasonic inspection monitor (Figure 3c). In the measurement, the sampling frequency is set to 10 MHz, the sensor frequency is 35 kHz, and the butter coupling is adopted between the sample and the sensor. Table 1 shows that the density of a water-saturated sample is 2.66 g/cm^3, 25.5% higher than that of a dry sample, and the longitudinal wave velocity of a water-saturated sample is 3154 m/s, 23.0% higher than that of a dry sample. In water, the water molecules fill the pores inside the sample, increasing the density of the sample and increasing the speed of the P wave propagation through the sample.

3.2. Test Methods. An RMT-150B electrohydraulic servo rock test system (Figure 4) was used to conduct uniaxial compression tests and conventional triaxial compression tests on dry samples and water-saturated samples to test the changes in the mechanical properties of the samples under different water conditions. During the test, the axial load was measured using a 1000 kN force transducer, and the axial compression deformation was measured using a 5.0 mm displacement transducer.

3.2.1. Uniaxial Compression Test. The uniaxial compression testing adopted displacement loading, and the loading rate was 0.005 mm/s. The whole stress–strain curve of the sample during loading was obtained to determine the impact energy index of the sample, and the changes in the rockburst tendency of the sample under different water conditions were explored.

3.2.2. Conventional Triaxial Compression Test. The triaxial compression testing was carried out in five groups with three samples in each group. The confining pressure of each group was set at 3, 6, 9, 12, and 15 MPa. The axial pressure was loaded in displacement mode with a loading rate of 0.005 mm/s.

3.3. Test Results and Analysis

3.3.1. Uniaxial Compression Test. Figure 5a shows the stress–strain curves of typical samples in each group under uniaxial compression. Figure 5a shows that the uniaxial strength of the water-saturated sample is 37.3 MPa, 34.8% lower than that of the dry sample (57.2 MPa), indicating that the water-saturated sample has a certain deterioration effect on the strength of the sample. To calculate the energy variation of the sample during loading, the stress–strain curve (σ–ε curve) was converted into a force–displacement curve (F–x curve), as shown in Figure 5b,c.

According to physics, when a constant force works, the energy calculation formula is as follows:

$$W = Fx. \tag{1}$$

In uniaxial compression experiments, the indenter is loaded with constant displacement, and the force is not constant. Taking Figure 5b as an example, to calculate the energy stored in the sample during loading, the calculus method can be adopted:

$$W_1 = \int_0^{x_c} F(x)dx, \tag{2}$$

where W_1 is the energy accumulated during the loading process of the sample and x_c is the strain at the peak stress. Since the function expression of $F(x)$ is unknown, Equation (2) cannot be solved directly. Here, we first introduce an infinitely small quantity ($\triangle x$), divide the $F(x)$ curve into infinitely small rectangles, and calculate the sum of the areas of each small rectangle:

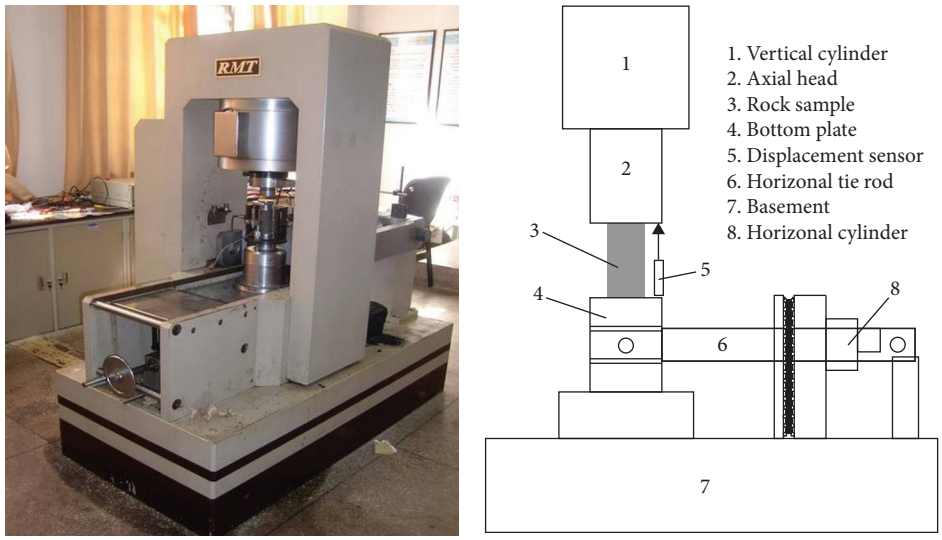

(a) (b)

FIGURE 4: An RMT-150B electrohydraulic servo rock testing system was used: (a) testing device and (b) uniaxial compression schematic.

$$W_1 = \int_0^{x_c} F(x)dx = \sum_{n=0}^{x_c} \triangle x \cdot \frac{[F(n) + F(n+\triangle x)]}{2}, \quad \begin{cases} n = m \cdot \triangle x \\ m \in N \text{ (Number set)} \end{cases}. \tag{3}$$

Likewise,

$$W_2 = \int_{x_c}^{x_e} F(x)dx = \sum_{n=x_c}^{x_e} \triangle x \cdot \frac{[F(n) + F(n+\triangle x)]}{2}, \tag{4}$$

where W_2 is the energy released after the sample is destroyed.

Then, the impact energy index K_E is as follows:

$$K_E = \frac{W_1}{W_2}. \tag{5}$$

According to Equations (3)–(5), the accumulated or released energy of the sample in the uniaxial compression process is calculated, as shown in Figure 6.

As shown in Figure 6, the peak value of the energy change in the dry sample is mainly concentrated from the end of the elastic stage to the yield failure stage, while the energy distribution of the water-rich sample is more uniform, reaching its maximum at the peak point of the stress–strain curve and gradually decreasing to both sides. The impact energy indices of the water-rich samples are 1.178% and 57.2% lower than that of the dry sample (2.755), indicating that the dry sample has a greater rockburst proneness.

The impact energy index plays a critical role in determining the fracture behavior and energy dissipation characteristics of rock under dynamic loading conditions. A higher impact energy index is often associated with increased fragmentation, making the rock more susceptible to breakage and potentially more brittle in nature. The rock's ability to absorb and dissipate energy is also affected, typically leading to reduced elasticity and increased permanent deformation. Consequently, variations in the impact energy index are crucial in the prediction and mitigation of slope-related hazards. Understanding the evolution of the impact energy index in slope rock masses under different conditions is significant for the study of slope stability.

3.3.2. Triaxial Compression Test. Figure 7 shows the stress–strain curves of typical samples in each group under triaxial compression. As shown in Figure 7, the samples in each group experience four stages: compaction, elastic deformation, plastic deformation, and failure. When the confining pressure is 3 MPa, the dry and water-rich samples exhibit obvious stress drops after reaching the peak value, revealing certain brittle failure characteristics. With increasing confining pressure, the peak strength and peak strain (the strain corresponding to the peak strength) of the sample also gradually increase, and the downward trend of the stress–strain curve tends to increase gradually after reaching the peak.

This indicates that with increasing confining pressure, the sample moves from brittle to plastic. Moreover, by comparing the postpeak phase of the stress–strain curves of the two groups of samples, the water-rich sample has obvious postpeak jitter compared with the dry sample, and the stress–strain curve mostly shows a trend of oscillatory change after the peak, which indicates that the samples in the water-rich area are less brittle and more plastic.

By analyzing the strength characteristics of the samples in each group, it can be seen that the peak strength of the dried samples under a confining pressure of 3 MPa is 80.6 MPa. Compared with the peak strength of the samples under a confining pressure of 3 MPa, the peak strengths of the dried samples under confining pressures of 6, 9, 12, and

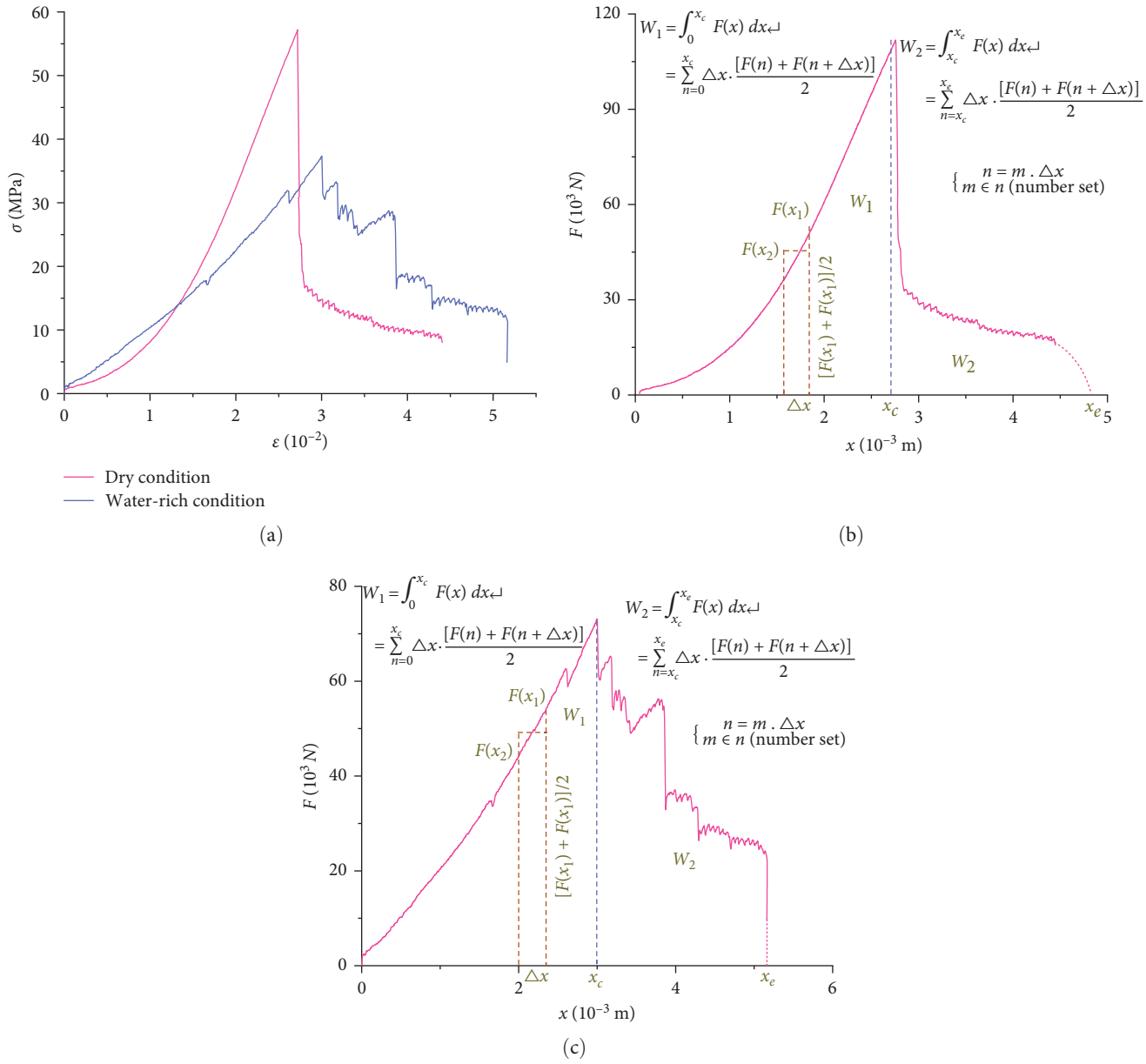

FIGURE 5: Uniaxial compression test curve: (a) σ–ε, (b) F–x under dry conditions, and (c) F–x under water-rich conditions.

15 MPa increase by 13.8%, 37.4%, 46.7%, and 55.8%, respectively. Compared with that of the dry samples, the strength of the water-rich samples decreases significantly, and the peak strength of the water-rich samples decreases by 28.5% on average under different confining pressure conditions, revealing obvious deterioration characteristics.

The peak strength σ_1 and confining pressure σ_3 of the two groups of samples are fitted, and the result conforms to the Coulomb strength criterion, as shown in Figure 8. Figure 8 shows that σ_1 and σ_3 are linearly related. The influence coefficient of the confining pressure on the dry samples is approximately 4.9, and the correlation coefficient is 0.98. The influence coefficient of the confining pressure on the water-rich samples is approximately 3.34, and the correlation coefficient is 0.99, indicating that the peak strength of triaxial compression on each sample is strongly correlated with the confining pressure.

According to the Coulomb strength criterion,

$$\sigma_1 = k\sigma_3 + Q, \tag{6}$$

where σ_1 is the peak intensity, σ_3 is the confining pressure, Q and k are material strength parameters, and the relationships between their values and the material's internal friction angle φ and cohesion force c are as follows:

$$\begin{cases} \varphi = \arcsin\left(\dfrac{k-1}{k+1}\right) \\ c = Q\left(\dfrac{1-\sin\varphi}{2\cos\varphi}\right) \end{cases}. \tag{7}$$

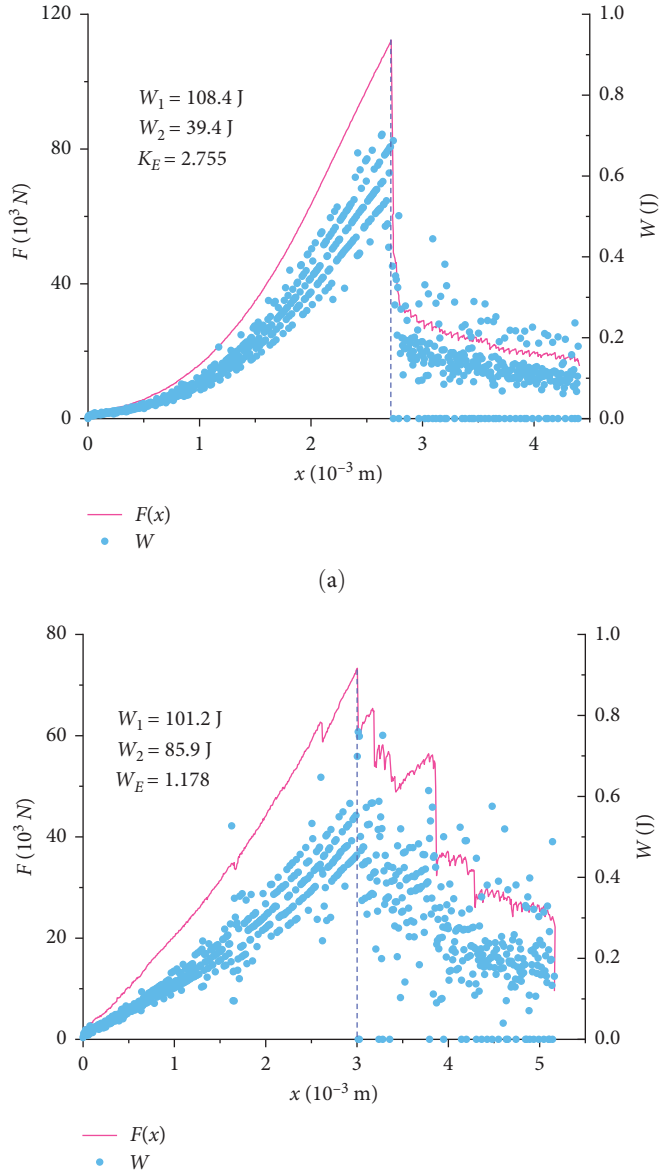

FIGURE 6: Impact energy index calculation: (a) dry conditions and (b) water-rich condition.

Figure 5 shows that the strength criterion of the sample used in this paper is as follows:

$$\begin{cases} \sigma_{1(1)} = 4.9\sigma_{3(1)} + 65.2 \\ \sigma_{1(2)} = 3.34\sigma_{3(2)} + 47.9 \end{cases}, \tag{8}$$

where subscript 1 indicates the dry sample and subscript 2 indicates the water-rich sample.

Namely,

$$\begin{cases} k_1 = 4.9, Q_1 = 65.2 \text{ MPa} \\ k_2 = 3.34, Q_2 = 47.9 \text{ MPa} \end{cases}. \tag{9}$$

By substituting Equation (4) into Equation (2), the cohesion and internal friction angle of the sample can be obtained:

$$\begin{cases} c_1 = 14.7 \text{ MPa}, \varphi_1 = 41.37° \\ c_2 = 13.1 \text{ MPa}, \varphi_2 = 32.63° \end{cases}. \tag{10}$$

According to the modified Coulomb strength criterion, they are as follows [33, 34]:

$$\sigma_t = \alpha \times \frac{2c \cdot \cos\varphi}{1 + \theta \sin\varphi} - \beta, \tag{11}$$

where $\alpha = 0.38$, $\beta = -5.2$, and $\theta = 0.1$.

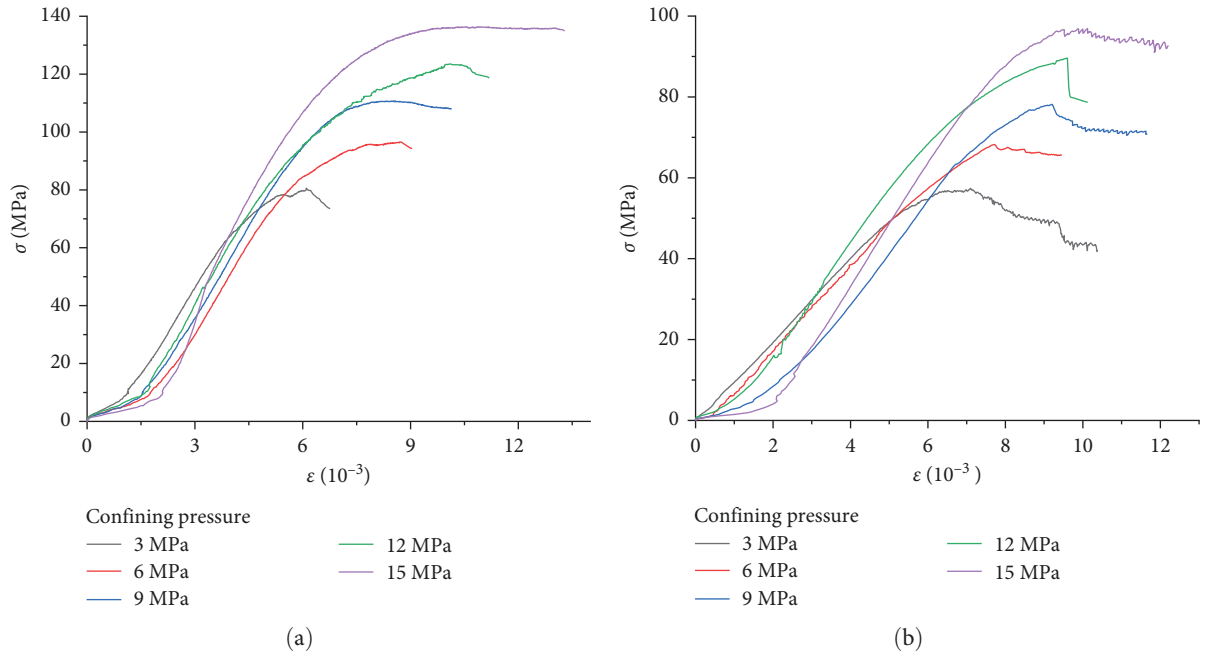

Figure 7: Triaxial compression experimental curve: (a) dry conditions and (b) water-rich conditions.

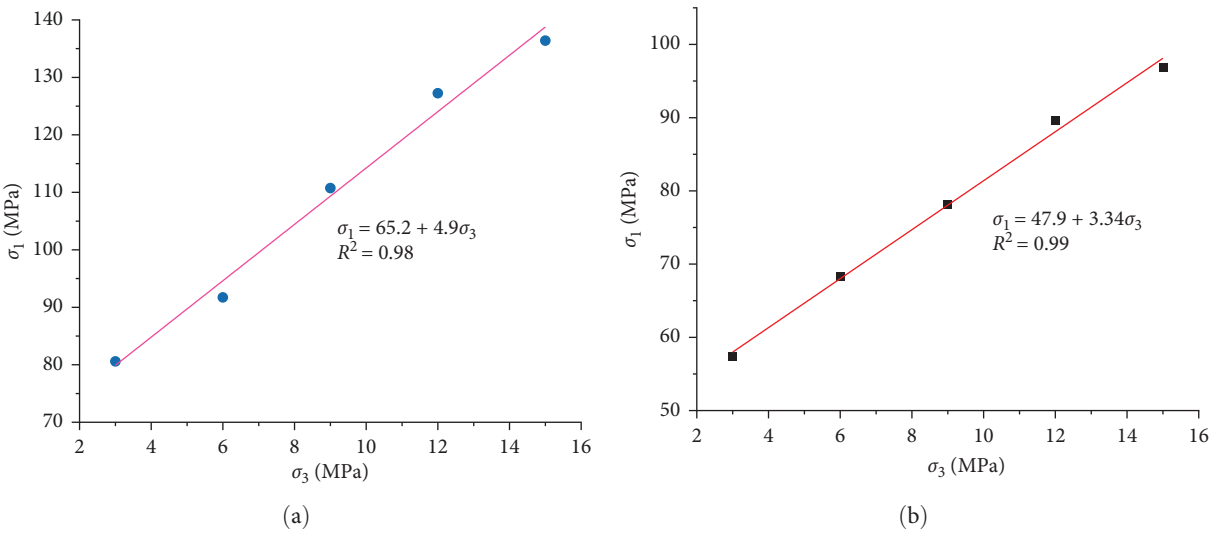

Figure 8: Relationship between peak intensity and confining pressure: (a) dry conditions and (b) water-rich conditions.

By substituting Equation (5) into Equation (6), the tensile strength of the sample can be obtained as follows:

$$\begin{cases} \sigma_{t(1)} = 5.27\ \text{MPa} \\ \sigma_{t(2)} = 4.25\ \text{MPa} \end{cases}. \tag{12}$$

Therefore, the mechanical parameters of a limestone slope corresponding to a landslide point in the study area used in this paper are shown in Table 2.

4. Slope Stability Study

4.1. Model Establishment. In this study, the strength reduction method was used to calculate the stability of slopes under different conditions. Therefore, FLAC3D software was used to model and analyze the slope. The established model is shown in Figure 9. The model parameters are shown in Table 1. In the model, the S1 and S2 measurement points were set up from the foot of the slope to the right. Both measuring points are inflection points of the profile.

Table 2: Mechanical parameters of the specimens.

	σ_3 (MPa)	σ_1 (MPa)	c (MPa)	φ (degree)	σ_c (MPa)	σ_t (MPa)
Dry	3	80.6	14.7	41.37	65.2	5.27
	6	91.7				
	9	110.7				
	12	127.2				
	15	136.4				
Water-rich	3	57.4	13.1	32.63	47.9	4.25
	6	68.3				
	9	78.1				
	12	89.6				
	15	96.9				

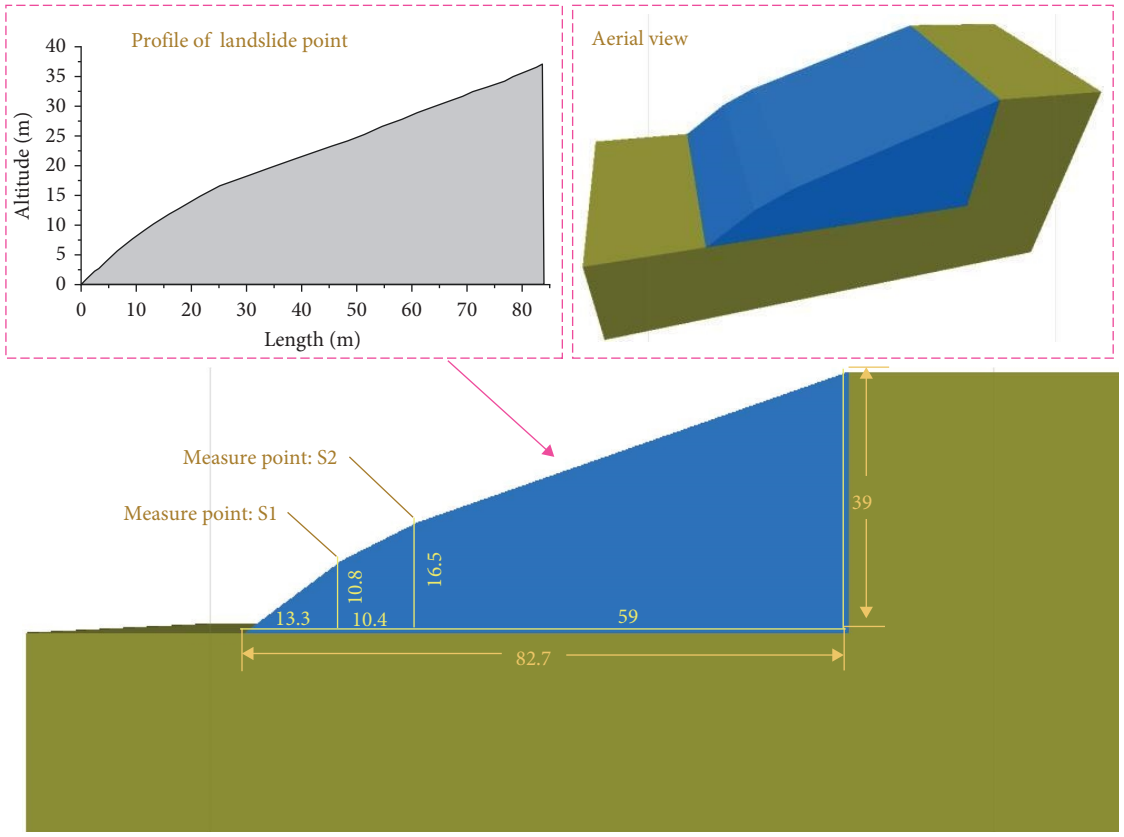

Figure 9: Typical section of the slope mining area of the landslide point.

4.2. Stability Analysis of Slopes Under Static Load Drying Conditions. The calculated results of the slope of the landslide point under dry and water-rich conditions are shown in Figures 10 and 11.

According to Figure 10, the shear strain in the *XZ* direction of the slope surface is mainly concentrated in the lower part of the slope under dry conditions, with a maximum value of 3.38×10^{-5}. The distribution of the plastic zone is mainly concentrated at position A at the lower part of the slope and position B at the upper part of the slope. Tensile plastic deformation occurs at position B at the top during the calculation process, while shear and tensile plastic deformation occur at position A in the lower part. However, with the equilibrium of the model calculation, both areas tend to be stable. This shows that the stability of the slope is better under dry conditions and that the stress concentration area and plastic deformation area of the slope surface are mainly concentrated at positions A and B. Therefore, in the daily protection stage, attention should be given to strengthening the protection of these two locations.

Figure 11 shows that the shear strain in the *XZ* direction on the slope surface is also mainly concentrated in the lower part of the slope under water-rich conditions, and the maximum value is 5.02×10^{-5}, which is 48.5% greater than that

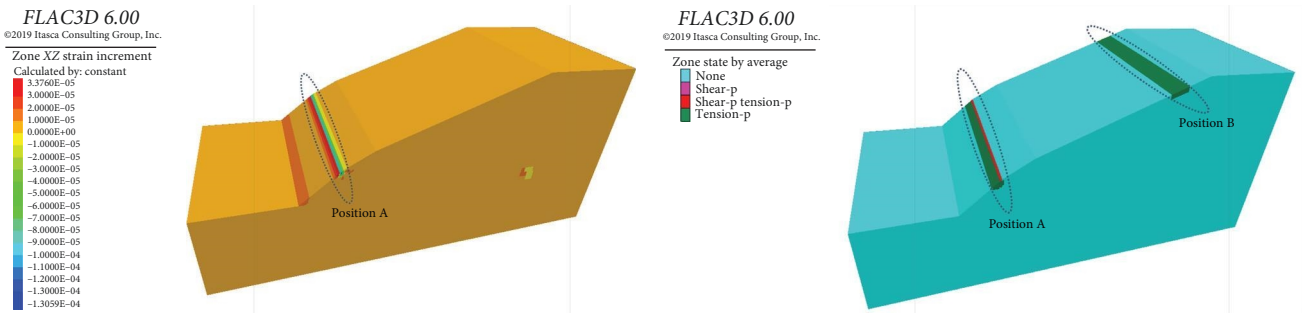

Figure 10: Strain and stress state contour maps of typical landslide sections in the study area under dry conditions: (a) strain in the *XZ* direction and (b) stress state.

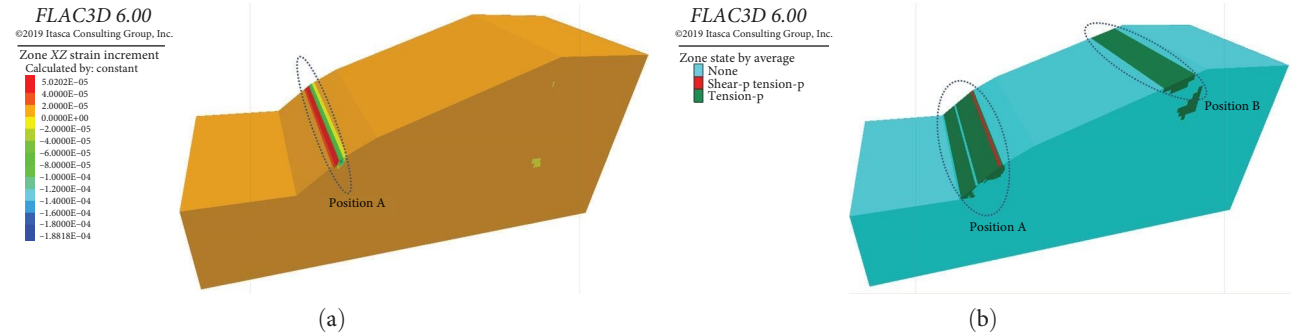

Figure 11: Strain and stress state contour map of typical landslide sections in the study area under water-rich conditions: (a) strain in the *XZ* direction and (b) stress state.

under dry conditions (3.38×10^{-5}). The plastic zone is also distributed around two positions, A and B; however, the range of the plastic zone is obviously larger under water-rich conditions than that under dry conditions, and the top of the slope is in the tensile failure zone from the lower position A to the bottom of the slope. The changes in the strain and plastic zone indicate that the stability of the slope is greatly reduced under water-saturated conditions, and position A at the lower part of the slope is in an unstable state due to the large stress concentration. Therefore, the monitoring and protection of position A of the water-saturated slope should be strengthened.

4.3. Calculation of the Safety Factor of Slopes Under Different Conditions

4.3.1. Principle of Intensity Reduction. Section 4.2 analyzes the stability of slopes under static load drying conditions. Based on Section 4.2, this chapter uses FLAC^{3D} software and the strength reduction method to calculate and analyze the safety factor of landslide slopes. The flow chart is shown in Figure 12. The cohesion and internal friction angle of a slope are closely related to its stability. The greater these values, the more stable the slope tends to be; conversely, lower values make the slope more prone to instability. The strength reduction method we employed focuses precisely on these parameters. By progressively reducing the cohesion and internal friction angle of the rock and soil mass in the slope, we aim to identify the slope's limit equilibrium state. This process of systematically decreasing cohesion and the internal friction angle is referred to as "reduction." After the reduction of the soil shear strength, the parameters may be defined as follows:

$$\begin{cases} c' = \dfrac{c}{F^{\text{trial}}} \\ \varphi' = \arctan\left(\dfrac{\tan\varphi}{F^{\text{trial}}}\right) \end{cases}, \tag{13}$$

where c' and φ' are the reduced shear strength parameters and F^{trial} is the reduction coefficient.

The safety factors of slope engineering designs under different conditions are shown in Table 3 [35, 36]. In Table 3, load combination I is "deadweight and groundwater"; load combination II is "deadweight, groundwater, and blasting vibration force"; and load combination III is "deadweight, groundwater, and seismic force."

4.3.2. Safety Factor of Slopes Under Different Conditions. Referring to Table 2 and the actual situation of the slope, the stability of the slope is calculated under the three conditions of "dry and deadweight," "water-rich and deadweight," and "water-rich and earthquake." Then, the c and φ values of the landslide under each condition are reduced according to the workflow in Figure 12.

The reduction coefficients of the three conditions are as follows:

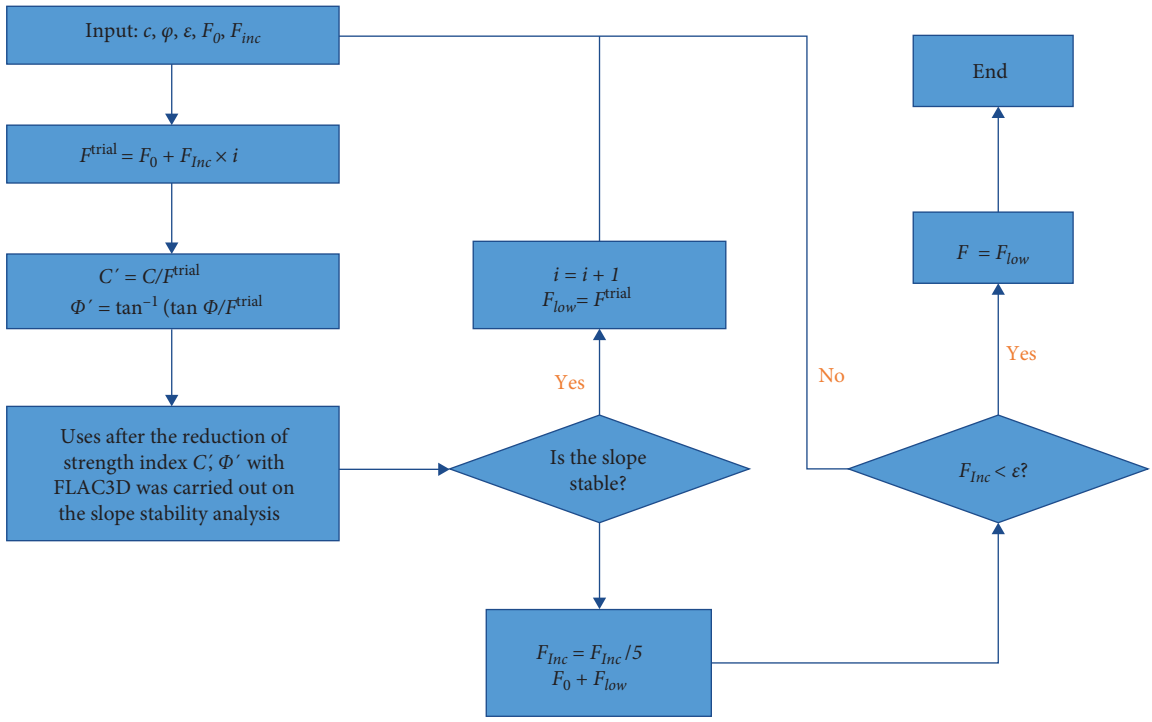

Figure 12: Flowchart of the intensity reduction method.

Table 3: Design safety factor of the overall slope under different load combinations (the table is reproduced from literature [35]).

Slope engineering safety level	Safety factor of slope engineering design		
	Load combination I	Load combination II	Load combination III
I	1.25–1.20	1.23–1.18	1.20–1.15
II	1.20–1.15	1.18–1.13	1.15–1.10
III	1.15–1.10	1.13–1.08	1.10–1.05

$$\begin{cases} F^{trial} = \{1.20, 1.21, 1.22, 1.23, 1.24, 1.25\} \\ F^{trial} = \{1.18, 1.19, 1.20, 1.21, 1.22, 1.23\}. \\ F^{trial} = \{1.15, 1.16, 1.17, 1.18, 1.19, 1.20\} \end{cases} \quad (14)$$

By substituting Equation (14) into Equation (13), the reduced values of c and φ can be obtained under the three conditions.

By writing the reduced values of c and φ into the Flac3D command stream, the reduced maximum imbalance inside the monitoring curve can be obtained. When the maximum imbalance force ratio n is less than 1×10^{-5}, the slope is considered to be stable; otherwise, it is considered to be unstable.

Figure 13 shows the relationship curve between the scale coefficient n of stability and the reduction coefficient F^{trial} at the landslide point.

In Figure 13, the coordinates corresponding to the red line are $n = 10^{-5}$. According to the figure, the safety factor of the slope under the conditions of "dry and deadweight" was 1.231. Under the conditions of "water-rich and deadweight," the safety factor of the landslide slope was 1.193, which was

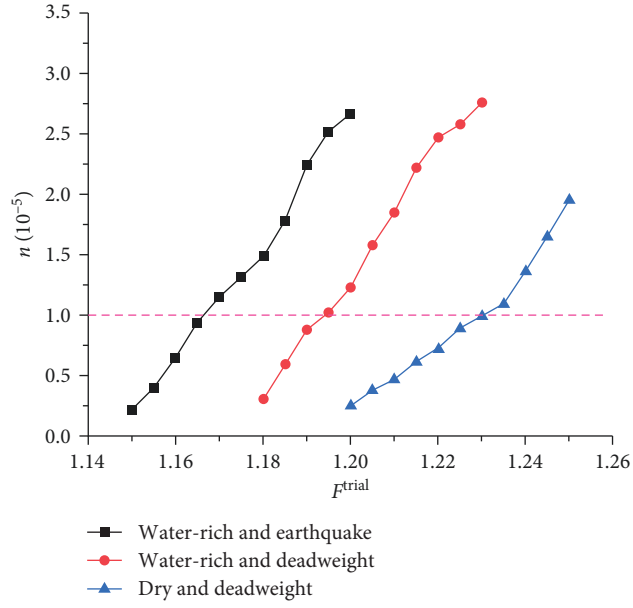

Figure 13: Proportional coefficient of slope stability at the slope under three conditions.

3.1% lower than that under the "dry and deadweight" conditions. Under the conditions of "water-rich and earthquake," the safety factor of the landslide slope was 1.165, which was 5.4% lower than that under the conditions of "dry and deadweight." Both "water-rich" and "earthquake" conditions can cause a decrease in the safety factor of landslide slopes. The landslide slopes are in the Huaying Mountain seismic belt and often experience rainy weather, during which water accumulation often occurs. Therefore, the management and protection of water-rich areas of slopes should be strengthened.

The unique topography, geological structure, and lithology of the landslide points in the study area provide internal conditions for the sliding body to travel. The external factors inducing landslides are mainly rainfall and seismic activity. Different influencing factors are combined, the numerical simulation of the landslide area is carried out, and the stability of the landslide is analyzed according to the results. Under the conditions of "dry and deadweight," the safety factor is 1.231, the whole landslide body is in a relatively stable state, and it is not easy to destabilize and deform. For the simulated safety factor under the conditions of "water-rich and deadweight" 1.193, it indicates that under the influence of precipitation, the water content of the rock mass increases, the weight of the slope increases, and its stability decreases, increasing instability and deformation. Under the "water-rich and earthquake" conditions, the safety factor is 1.165, and its stability is the worst among the cases studied. Under continuous rainfall conditions, water stagnation easily occurs, slope saturation occurs, and the water content of the slope increases. Under the action of seismic stress, a slope easily experiences deformation and instability slip under these conditions.

5. Conclusion

In this study, the stability of a side slope in Xingwen County is studied via field investigations, laboratory experiments, and numerical simulations. The conclusions are as follows:

1. The uniaxial strength of the samples in the water-rich zone is 34.8% lower than that in the dry zone, but the impact energy index of the samples is 57.2% lower than that in the dry zone. A high amount of water will lead to a decrease in rock strength and a tendency toward rockburst.
2. Compared with that of the dry sample, the strength of the water-rich sample decreased significantly, and the peak strength decreased by 28.5% on average under different confining pressure conditions. The stress–strain curve of the water-rich sample has more jitter after the peak and shows more obvious plastic characteristics. This indicates that water saturation has an obvious deterioration effect on the slope rock mass.
3. The peak shear strain in the *XZ* direction on the lower slope under water-rich conditions is 48.5% greater than that under dry conditions, and the range of the slope plastic zone under water-rich conditions is also significantly greater than that under dry conditions. The changes in the strain and plastic zone show that the stability of the slope under water-rich conditions is much lower than that under dry conditions.
4. The safety factor of the slope under the conditions of "dry and deadweight" is the highest, while the safety factors of the slope under the conditions of "water-rich and deadweight" and "water-rich and earthquake" are reduced by 3.1% and 5.4%, respectively. The landslide slope is in the Huaying Mountain seismic belt and is often in rainy weather, and water accumulation often occurs on the slope. Therefore, it is necessary to strengthen the management and protection of water-rich areas in areas with frequent microearthquakes.

Data Availability Statement

The data that support the findings of this study are available from the corresponding author upon reasonable request.

Conflicts of Interest

The authors declare no conflicts of interest.

Author Contributions

Chongyang Wang supervised the research and proposed the research direction. Shujian Li was responsible for the report analysis and writing of the paper. Yisha Pan, Dongming Zhang, Bin Zhang, and Ziyang Xiong helped write the paper.

Funding

This work was supported by the Yunnan phosphorus resources technology innovation center (Project Approval Number: 202305AK340002) and the State Key Lab of Coal Mine Disaster Dynamics and Control (Project Approval Number: 2011DA105287-zd201804).

References

[1] X. Shao, S. Ma, C. Xu, L. Shen, and Y. Lu, "Inventory, Distribution and Geometric Characteristics of Landslides in Baoshan City, Yunnan Province, China," *Sustainability* 12, no. 6 (2020): 2433.

[2] W. Shabbir, T. Omer, and J. Pilz, "The Impact of Environmental Change on Landslides, Fatal Landslides, and Their Triggers in Pakistan (2003–2019)," *Environmental Science and Pollution Research International* 30, no. 12 (2023): 33819–33832.

[3] R. Ramanathan, A. Aydilek, and B. Tanyu, "Development of a GIS-Based Failure Investigation System for Highway Soil Slopes," *Frontiers of Earth Science* 9, no. 2 (2015): 165–178.

[4] W. J. Randall and L. H. Edwin, "Ground Motions at the Outermost Limits of Seismically Triggered Landslides," *Bulletin of the Seismological Society of America* 2, no. 106 (2016): 708–719.

[5] K. Sampath, M. Perera, D. Elsworth, P. Ranjith, S. Matthai, and T. Rathnaweera, "Experimental Investigation on the Mechanical Behavior of Victorian Brown Coal under Brine Saturation," *Energy & Fuels* 32, no. 5 (2018): 5799–5811.

[6] Y. Chen, L. Zhao, Y. Wang, Q. Jiang, and D. Qi, "Precipitation Data and Their Uncertainty as Input for Rainfall-Induced

Shallow Landslide Models," *Frontiers of Earth Science* 13, no. 4 (2019): 695–704.
[7] S. Liu, H. Wang, W. Xu, Z. Cheng, Z. Xiang, and W.-C. Xie, "Numerical Investigation of the Influence of Rock Characteristics on the Soil-Rock Mixture (SRM) Slopes Stability," *KSCE Journal of Civil Engineering* 24, no. 11 (2020): 3247–3256.
[8] H. Tanyaş and L. Lombardo, "Variation in Landslide-Affected Area under the Control of Ground Motion and Topography," *Engineering Geology* 260 (2019): 105229.
[9] O. Marc, P. Meunier, and N. Hovius, "Prediction of the Area Affected by Earthquake-Induced Landsliding Based on Seismological Parameters," *Natural Hazards and Earth System Science* 17, no. 7 (2017): 1159–1175.
[10] B. Li and F. Zhang, "Three-Dimensional Stability Evaluation of Shallow Loess Landslide under Rainfall and Seismic Conditions," *Chinese Journal of Engineering* 44, no. 3 (2022): 440–450.
[11] J. Tan, B. Horsfield, R. Fink, et al., "Shale Gas Potential of the Major Marine Shale Formations in the Upper Yangtze Platform, South China, Part III: Mineralogical, Lithofacial, Petrophysical, and Rock Mechanical Properties," *Energy & Fuels* 28, no. 4 (2014): 2322–2342.
[12] V. Senthilkumar, S. S. Chandrasekaran, and V. B. Maji, "Rainfall-Induced Landslides: Case Study of the Marappalam Landslide, Nilgiris District, Tamil Nadu, India," *International Journal of Geomechanics* 18, no. 9 (2018): 05018006.
[13] C. Qin and S. C. Chian, "New Perspective on Seismic Slope Stability Analysis," *International Journal of Geomechanics* 18, no. 7 (2018): 06018013.
[14] C. Xu, T. Gorum, and H. Tanyas, ", Editorial: Application of Remote Sensing and GIS in Earthquake-Triggered Landslides," *Frontiers in Earth Science* 10 (2022): 964753.
[15] C. Wu, "Landslide Susceptibility Based on Extreme Rainfall-Induced Landslide Inventories and the Following Landslide Evolution," *Water* 11, no. 12 (2019): 2609.
[16] J. Samia, A. Temme, A. Bregt, et al., "Do Landslides Follow Landslides? Insights in Path Dependency From a Multi-Temporal Landslide Inventory," *Landslides* 14, no. 2 (2017): 547–558.
[17] F. Zhao, S. Yu, B. Li, and Z. Shi, "Research Advances on Large-Scale Shaking Table Test for Rock Slopes under Earthquake," *Earth Science* 47, no. 12 (2022): 4498–4512.
[18] W. Zhang, R. Yu, Y. Chen, Y. Gao, and Y. Huang, "Influence of Strength Index on the Motion Characteristics and Parameter Inverse Analysis of Landslide," *Chinese Journal of Geotechnical Engineering* 44, no. 12 (2022): 2304–2311.
[19] Z. Ma, B. Zhu, H. Wu, et al., "Experimental Study on Seismic Failure Characteristics Optimization of Landslide-Tunnel Seismic Absorption Based on Energy Analysis," *Chinese Journal of Rock Mechanics and Engineering* (2023): 1–16.
[20] L. Pai and H. Wu, "Experimental Study on Dynamic Response of Tunnel Orthogonal Downslide Lining Structure," *Chinese Journal of Rock Mechanics and Engineering* 41, no. 5 (2022): 979–994.
[21] M. Son and S. Adedokun, "Effect of Joint Inclination Angles on the Earth Pressure Against the Support System in a Jointed Rock Mass," *KSCE Journal of Civil Engineering* 20, no. 4 (2016): 1259–1266.
[22] M. Son and S. Adedokun, "Earth Pressure on a Retaining Structure in Layered and Jointed Rock Masses," *KSCE Journal of Civil Engineering* 21, no. 4 (2017): 1147–1153.
[23] W. Wu, F. Gong, Q. Jiang, and L. He, "Strength Reduction of Initial High-Stress Rock Pillars Under Different Triaxial Unloading Paths," *Rock Mechanics and Rock Engineering* 56 (2023): 3519–3537.
[24] H. Zhou, A. Che, and R. Zhu, "Damage Evolution of Rock Slopes Under Seismic Motions Using Shaking Table Test," *Rock Mechanics and Rock Engineering* 55, no. 8 (2022): 4979–4997.
[25] Z. Chen, P. Yang, W. Tong, and H. Liu, "Model Test Study on the Influence of Earthquake on the Morphology of Bulk Landslide Accumulation," *Journal of Disaster Prevention and Mitigation Engineering* 41, no. 2 (2021): 211–220.
[26] Y. Wu, H. Zhou, and A. Che, "Study on Susceptibility of IBURI Earthquake Landslides Based on rough Set-Neural Network," *Chinese Journal of Rock Mechanics and Engineering* 40, no. 6 (2021): 1226–1235.
[27] J. Li, "Stability Analysis and Simulation of Loess Landslide," *China University of Geosciences* (2021).
[28] Y. Pan, C. Wang, and Y. Wang, "Mechanical Degradation Mechanism of Rock under Seismic Disturbance Stress," *Quarterly Journal of Engineering Geology and Hydrogeology* 55, no. 4 (2022): qjegh2022-007.
[29] G. Wang, H. Li, Y. Tian, et al., "Study on Genetic Mechanism and Risk Prediction of Typical High Accumulation Bed Landslide in Bailong River Basin, Gansu Province," *Chinese Journal of Rock Mechanics and Engineering* 4 (2023): 1–16.
[30] J. Broeckx, M. Vanmaercke, R. Duchateau, and J. Poesen, "A Data-Based Landslide Susceptibility Map of Africa," *Earth-Science Reviews* 185 (2018): 102–121.
[31] C. Yang, J. Zhang, F. Liu, J. Bi, and Z. Jun, "Analysis on Two Typical Landslide Hazard Phenomena in the Wenchuan Earthquake by Field Investigations and Shaking Table Tests," *International Journal of Environmental Research and Public Health* 12, no. 8 (2015): 9181–9198.
[32] S. Guan, H. Jiang, X. Lu, et al., "Strike-Slip Fault System and Its Control on Oil & Gas Accumulation in Central Sichuan Basin," *Acta Petrolei Sinica* 43, no. 11 (2022): 1542–1557.
[33] C. Wang, S. Wei, D. Zhang, Y. Yang, B. Yu, and Y. Pan, "Physical Properties and Tensile Strength Evolution of Gypsum Materials under Different Water Content Conditions," *Construction and Building Materials* 364 (2023): 129865.
[34] C. Wang, D. Zhang, B. Yu, and S. Li, "Deformation and Seepage Characteristics of Coal under True Triaxial Loading-Unloading," *Rock Mechanics and Rock Engineering* 56, no. 4 (2023): 2673–2695.
[35] S. Wu, P. He, H. Cheng, G. Wang, X. Zhang, and Z. Zhang, "Discussion on the Stability Evaluation Standard of a Rock Slope in a Noncoal Open-Pit Mine," *Chinese Journal of Engineering* 44, no. 5 (2022): 876–885.
[36] GB 51016-2014, "Technical Code for Non-Coal Open-Pit Mine Slope Engineering".